Ferromagnetism observed in silicon-carbide-derived carbon

Bo Peng, Yuming Zhang, Yutian Wang, Hui Guo, Lei Yuan, and Renxu Jia*

School of Microelectronics, Key Laboratory of Wide Band-Gap Semiconductor Materials and Devices, Xidian University, Xi'an 710071, China

(Received 4 February 2017; revised manuscript received 8 January 2018; published 1 February 2018)

Carbide-derived carbon (CDC) is prepared by etching high purity 4H-SiC single crystals in a mixed atmosphere of 5% Cl_2 and 95% Ar for 120 min and 240 min. The secondary ion mass spectroscopy (SIMS) bulk analysis technique excludes the possibility of ferromagnetic transition metal (TM) contamination arising during the experimental process. The paramagnetic and ferromagnetic components are separated from the measured magnetization-magnetic field curves of the samples. Through the use of the Brillouin function, paramagnetic centers carrying a magnetic moment of $\sim$1.3 μ_B are fitted. A resolvable hysteresis loop in the low magnetic field area is preserved at room temperature. The temperature dependence of the relative intensity of the Lorentzian-like electron spin resonance (ESR) line observed by electron spin spectroscopy reveals the existence of exchange interaction between the localized paramagnetic centers. First-principles calculations show the dominant configuration of defects in the graphitic CDC films. By calculating the energy difference between the antiferromagnetic and ferromagnetic phases, we deduce that the ferromagnetic coupling is sensitive to the concentration of defects.

DOI: 10.1103/PhysRevB.97.054401

I. INTRODUCTION

The discovery of transition metal (TM)-free ferromagnetism in several carbon-based materials, such as irradiated or implanted graphite [1–4], graphene [5,6], C_{60} polymers [7–10], and amorphous carbon [11–19], for which the saturation magnetization ranged substantially, has inspired a number of researchers to study the novel and confusing physical mechanism behind it. These discoveries have greatly extended researchers' perspective and have promoted these electronic functional materials as candidates in spintronic and biomedical applications.

In fact, paramagnetic centers composed of neutral, charged, or atom adsorption defects are crucial for the observed ferromagnetism in graphite and graphene layers. For example, Yazyev and Helm [20] demonstrated that point defects carrying magnetic moments are necessary for the ferromagnetic or antiferromagnetic ordering of graphene. In addition, several scientists [21–23] have proved that hydrogen- and nitrogen-adsorption vacancies play pivotal roles in the ferromagnetism in defective graphite through theoretical calculations.

Moreover, the mechanisms by which these paramagnetic centers couple together to create ferromagnetism at certain temperatures have been studied, and several models, such superexchange mediated by two different sites [20], direct exchange coupling [24] and hydrogen adsorption enhanced electron-mediated coupling [25], have been proposed by different research groups to explain the observed results. In addition to the theoretical studies, x-ray magnetic circular dichroism (XMCD) spectroscopic analysis proves that the carbon π states in defective ferromagnetic graphite exhibit a net spin polarization [23]. These interesting features provide a route to link TM-free ferromagnetism with the defective sp^2 skeleton in carbon-based materials.

For amorphous carbon, ferromagnetic order with a broad range of saturation magnetizations and Curie temperatures has been observed in a variety of microstructures prepared by different physical and chemical methods. Table I lists the saturation magnetizations and the Curie temperatures of some amorphous carbon structures. There are several explanations for the increase in ferromagnetic coupling in these materials. Reference [13] noted that the ferromagnetic behavior of microporous carbon is governed by isolated clusters and suggested that the occurrence of a percolative-type transition with the temperature decrease. The existence of the π-type paramagnetic spins and the interaction between π- and σ-type spins were observed by electron spin resonance (ESR) spectroscopic analysis of carbon materials prepared from trialkylboranes with magnetic order [12]. Additionally, for a carbon nanofoam, a possible mechanism for magnetic moment generation would be a simple indirect exchange interaction through conduction electrons located on the hexagons [15].

Meanwhile, the debate over the contamination-induced ferromagnetism in these carbon-based materials is still a problem in this field. For instance, the main problem with the amorphous carbon prepared by the pyrolysis of some organic precursors in early works was the unclear contribution of magnetic impurities, which is determined by the purity of the chosen materials and the detection limit of the characterization method and may be introduced through the preparation procedure used [11,12]. Furthermore, the induction of the observed magnetic properties by ferromagnetic impurities in some articles can be precluded only by calculating and comparing the upper limit of the impurity concentration with the magnitude of the measured magnetization [13,16]; however, due to the grain size and distribution, the magnetic impurity always has a complicated influence on the magnetic properties of the observed samples [26]. The same

*rxjia@mail.xidian.edu.cn

TABLE I. The saturation magnetizations and the Curie temperatures of some amorphous carbon structures.

Materials	Saturation magnetization (emu/g)	Curie temperature (K)	Reference
Pyrolytic carbon	0.06 (4 K), 0.05 (260 K)	above 260	[11]
Microporous carbon	0.02 (5 K)	30	[13]
Carbon nanofoam	0.42 (1.8 K)	90	[15]
Carbon nanoparticles	0.93 (20 K), 0.90 (300 K)	above 300	[16]
Nanofluid magnetic graphite	0.0015 (2 K)	above 300	[17]
Sulfur-doped amorphous carbon powder	0.002 (5 K)	17	[18]
Carbon nanodisk and nanocone powders	0.006 (300 K)	above 300	[19]

problem was also found in conventional industrial graphite, which contains a small quantity of magnetic impurities, such as Fe and its compounds. As a contrary opinion, Nair *et al.* [27] reported that there is no ferromagnetism in the clean and well-characterized graphene laminates after introducing fluorine atoms or irradiation defects. Further work is still needed to prove the intrinsic ferromagnetism in carbon-based materials with high purity.

Carbon produced by selectively etching carbides is known as carbide-derived carbon (CDC) [28]. Silicon carbide is the most widely studied substrate for CDC growth since it is commercially available on a large scale and has numerous applications, ranging from power electronics to heavy-load bearings [29]. The most commonly used method to obtain CDC from SiC is through high-temperature chlorination [30]. According to previous investigations [31], the common well-prepared SiC-CDC exhibits an sp^2 carbon skeleton and complex defect configurations. Furthermore, the conventional industrial silicon carbide is well controlled with a high grade of purity, and thus, the use of 4H-SiC single crystals and grown CDC avoids the influence of magnetic impurities on magnetization measurements. In addition, compared with organic compounds, the 4H-SiC crystals used in our experiment were sliced into regular flakes, and the reaction occurred on the surfaces; in contrast to previous work [12], this treatment method will prevent the contact of the prepared amorphous carbon with the quartz tube. The high purity SiC-CDC will help us study the ferromagnetism in amorphous carbon and understand the effect of the defective planar sp^2 hybrid configuration on the magnetic properties of carbon-based materials.

In this paper, implementing the reaction of chlorine with 4H-SiC single crystals and high purity silicon CDC is reported. The structural and magnetic properties of the CDC are characterized, and ferromagnetic order is found. An investigation on the paramagnetic centers in the ferromagnetic samples is carried out by using electron spin resonance spectroscopy. Theoretical calculations are performed subsequently to investigate the localized paramagnetic centers and the interactions between them.

II. EXPERIMENTAL DETAILS

Two-side polished high-purity semi-insulating 4H-SiC single crystals from SICC Corporation (Shandong, China) were cut into pieces with dimensions of $4 \times 4 \times 0.35$ mm^3. Before heating and chlorinating, the samples were carefully cleaned by ultrasonic rinsing with acetone, alcohol, and deionized water. The samples were then placed in a quartz glass tube and heated at 10 °C/min up to 1100 °C. The surfaces of these samples were then exposed in a mixed atmosphere of 5% Cl_2 and 95% Ar with a flow rate of 20 sccm at 1100 °C for 30 min, 120 min, or 240 min (the chlorinated samples are hereafter referred to as S1, S2-1 and S2-2, and S3, respectively). Samples S2-1 and S2-2 were chlorinated under the same conditions but on two pristine wafers for comparison. During the total experimental time frame, the samples were carefully treated to prevent contamination from TM, for example, by avoiding contact with iron-containing tweezers. After chlorination, the samples were cooled to room temperature in high-purity argon. The chemical reaction that occurred during the experimental process can be described by Eq. (1):

$$SiC(s) + 2Cl_2(g) \rightarrow SiCl_4(g) + C(s). \quad (1)$$

The area of the CDC layer was estimated to be the same as that of the pristine SiC crystal (16 mm^2) because the reaction occurred on the entire surface region. The chlorination reaction rate of a SiC wafer in a chlorine atmosphere was found to be linear [29,32], and the kinetics can be described by the linear equation:

$$d = kt, \quad (2)$$

where d is the thickness of the CDC layer, t is the reaction time, and k is the linear reaction rate, which will increase exponentially with temperature. As an approximation, we calculated d from the above equation, and according to a previous study [29], the value of k at 1100 °C in 5% Cl_2 was estimated to be 1.00 μm/h. The volumes of the CDC layers were calculated by the product of area of the surface and the thickness d, and are used to deduce the normalized paramagnetic and ferromagnetic components in the samples. The total mass of the CDC samples was also measured in order to normalize the total magnetization because the diamagnetism mainly arose from the SiC substrates.

Here, the secondary ion mass spectroscopy (SIMS) bulk analysis technique was used to evaluate the CDC samples in order to exclude possible ferromagnetic TM contamination introduced during the experimental process. The amount of TM (Fe, Co, and Ni) and chlorine in one of the chlorinated samples (S3) was measured by Evans Materials Technology Co., Ltd. (Shanghai). For the measurement of iron, cobalt, and nickel, the primary ion is O^+ with a primary voltage of 12.5 kV, whereas for the measurement of Cl, the primary ion is Cs^+, and the primary voltage was set to 8 kV. The detection limits of iron, cobalt, and nickel concentrations in SIMS bulk analysis are 5×10^{13} atoms/cm^3, 5×10^{13} atoms/cm^3 and 1×10^{14} atoms/cm^3, respectively, when assuming a detection

TABLE II. Secondary ion mass spectroscopy bulk analysis results for sample S3 with a detection depth of ~10–20 μm.

Elements	Analysis 1 (atoms/cm^3)	Analysis 2 (atoms/cm^3)	Average (atoms/cm^3)
Fe	$<5 \times 10^{13}$	$<5 \times 10^{13}$	$<5 \times 10^{13}$
Co	$<5 \times 10^{13}$	$<5 \times 10^{13}$	$<5 \times 10^{13}$
Ni	$<1 \times 10^{14}$	$<1 \times 10^{14}$	$<1 \times 10^{14}$
Cl	$<1 \times 10^{15}$	$<1 \times 10^{15}$	$<1 \times 10^{15}$

depth of 10–20 μm. Table II shows the results of the SIMS bulk analysis of sample S3 as an example. The two analysis results and the average of the results in Table II indicate that contamination from Fe, Co, or Ni can be excluded within the detection limit of SIMS. The results in Table II also demonstrate that the concentration of chlorine in the chlorinated sample S3 is below the detection limit of SIMS bulk analysis as well, which excluded the possible influence of some attached chloride atoms on the experimental results.

The Raman spectra of the samples were collected by a μ-Raman spectroscopy (Renishaw inVia) by using a 532 nm wavelength Nd:YAG laser in the scattering geometry and with a power of 70 mW and an exposure time of 10 s. Magnetization-magnetic field curves were measured by a superconducting quantum interference device magnetic property measurement system magnetometer (SQUID-MPMS3, Quantum Design, Inc). ESR experiments were performed on JES-FA200 and Bruker E500 X-band ESR spectrometer. The FMR is measured using the NanOsc Instruments CryoFMR in a Quantum Design VersaLab System.

III. RESULTS AND DISCUSSION

A. Raman spectra

Figure 1(a) shows the Raman spectra for the high-purity semi-insulating 4H-SiC single crystal used as a precursor for the experiment and the chlorinated samples. The spectra were recorded at room temperature with the excitation laser perpendicular to the carbon face of the samples in the back scattering configuration. The instrument was calibrated with a silicon crystal. For the virgin sample, the major peaks located at 775 cm^{-1} and 963 cm^{-1} could be clearly observed, which are attributed to the folded transverse optic (FTO) and the longitudinal optic (FLO) modes, respectively, consistent with the results from other studies [33]. Some weak peaks are also observed in the area near 1500 cm^{-1} and 1700 cm^{-1}, which are assigned to the optical branches of the second-order Raman spectrum [34].

For chlorinated sample S1, the FTO and FLO modes mentioned previously can still be observed in the Raman spectrum; however, the decreasing scattering intensity reveals an increase in defect concentration after a 30 min chlorine etching. For samples S2-1, S2-2, and S3, the Raman scattering peaks located at 775 cm^{-1} and 963 cm^{-1} representing the characteristics of 4H-SiC are destroyed in the detected region. Instead, two peaks located at approximately 1330 cm^{-1} and 1610 cm^{-1} for samples S2-1 and S2-2 and at 1346 cm^{-1} and 1599 cm^{-1} for sample S3 with relatively strong intensities emerged in the spectra. The appearance of the new peaks indicates a pronounced conversion in the structure and composition in the chlorinated samples with the formation of CDC after a 240 min reaction. The peaks located at 1300–1350 cm^{-1} and 1580–1600 cm^{-1} are reported as D and G bands in other carbon based materials [30,31]. According to the previous results, the G band originates from the doubly degenerate phonon mode (E_{2g} vibration mode), which demonstrates the existence of in-plane sp^2 carbon sites. The width of the G band can be used to measure of quality of the formatted graphene planes [30]. The D band comes from the A_{1g}-ring breathing mode, the width of which is directly associated with the distribution of sp^2 bonded clusters with different ring sizes [35,36]. The D and G peaks in samples S2 and S3 show the formation of CDC in the chlorinated samples, and there is no obvious difference between the spectral shapes of sample S2-1 and S2-2, indicating that a stabilized and uniform etching environment has been used for the samples. Moreover, with increasing etching time, the widths of the G and D peaks of sample S3 become slightly narrower, which can be attributed to the more ordered graphitization.

The intensity ratio between the D and G peaks, which is proportional to the in-plane correlation length, is usually used to estimate in-plane crystallite sizes in CDC materials. The in-plane correlation length can be mathematically linked to the value of I_D/I_G by the T-K relationship [37]:

$$\frac{I_D}{I_G} = \frac{C(\lambda)}{L_a}, \tag{3}$$

where I_D and I_G are intensities of the D peak and G peak, respectively, L_a is the in-plane correlation length, and C(532nm) is approximately 4.96 nm. The value of I_D/I_G for sample S3 is 1.13, and the corresponding in-plane correlation length is calculated to be 4.39 nm. Ferrari and Robertson [31] classified disordered carbon-based materials with a three-stage model by analyzing the peak location and the values of I_D and I_G. According to their research results, CDC sample S3 lies in the stage near nanocrystalline graphite. The relationship between the density of defects and the intensity ratio between the D and G peaks in irradiated graphite was also studied by other authors [38], and for $I_D/I_G = 1.13$, the density of defects is approximately 7×10^{19} cm^{-3}, which is near the threshold of amorphization in graphite [39].

The peak located at approximately 2680 cm^{-1} that can be observed in our chlorinated samples S2-1, S2-2, and S3 is referred to as the 2D band, which is associated with the overtone of the D band. For bulk graphite, the 2D band can be decomposed into two peaks due to the two ordered stacking layers [40], but it is decreased and combined into a single weak peak when out-of-plane defects or crystalline damage between layers are induced. The 2D band observed in samples S2-1, S2-2, and S3 with a relatively weak intensity proves a disorder stacking of the sp^2 layer segments in our samples.

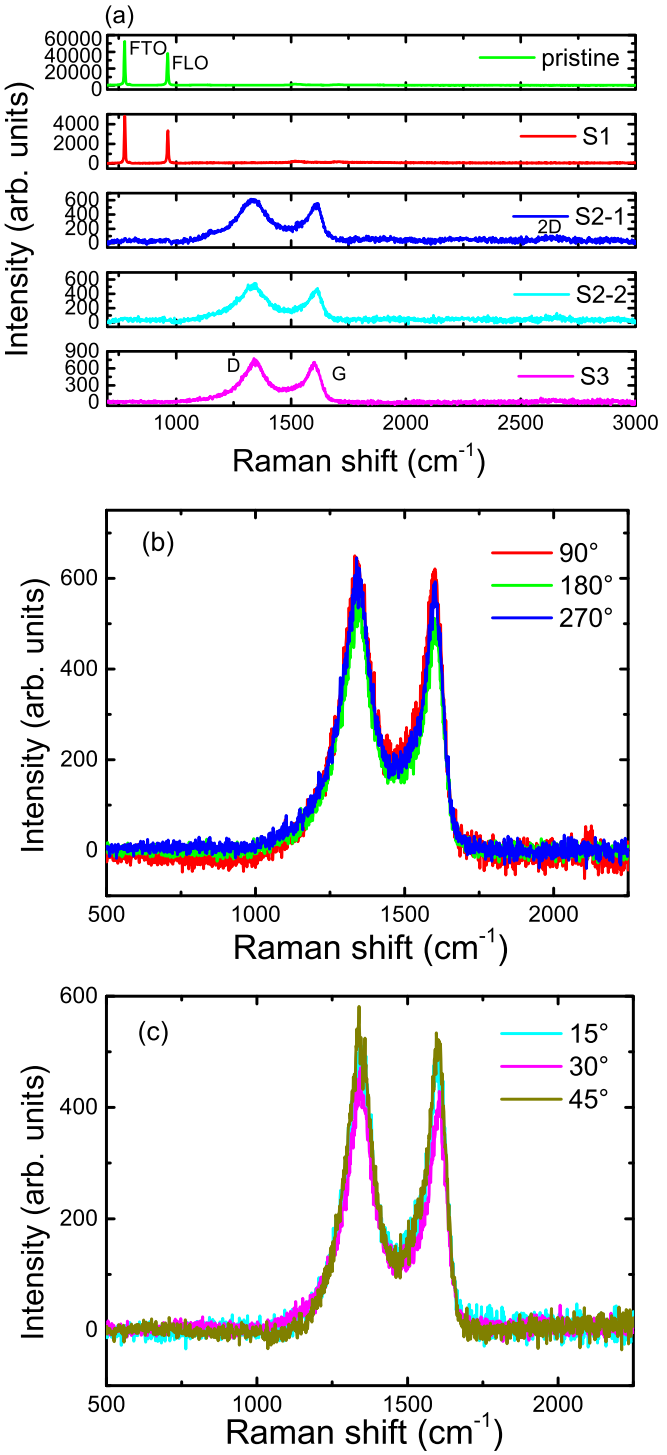

FIG. 1. (a) Raman spectra for the pristine and chlorinated 4H-SiC samples. The folded transverse optic (FTO) and longitudinal optic (FLO) modes of the pristine SiC sample and the D, G, and 2D peaks of CDC samples S2-1 and S3 are identified. A conversion in structure and composition could be observed in the chlorinated sample with an increase in etching time. (b) Raman spectra for the CDC sample S3 with in-plane rotation from 90° to 270°. (c) Raman spectra for CDC sample S3 with out-of-plane rotation from 15° to 45°.

To investigate the uniformity of our chlorinated samples, the Raman spectra with in-plane and out-of-plane rotation of the CDC sample are taken into consideration. Figure 1(b) displays the Raman spectra for sample S3 measured upon rotating the sample three times in-plane, from which the G and D peaks mentioned above could also be examined. The approximately equal intensity of each spectrum indicates an isotropic conformation of the CDC. Similarly, Figure 1(c) shows the Raman spectra for the three times out-of-plane rotation S3, an isotropic property could also be acquired from the intensities and the peaks of each spectrum. The results from the Raman spectra prove that the silicon atoms on the surface of the pristine 4H-SiC single crystal were gradually replaced by the chlorine along with the formation of uniformly distributed CDC.

B. Magnetization measurements

To study the magnetic properties of the samples, magnetization vs magnetic field curves were measured by a SQUID-MPMS3 device. The measured data already have the magnetic component of the plastic straw used for mounting samples subtracted out. Before discussing the magnetic properties of the CDC samples, the M-H curves of the pristine SiC sample measured at 5 K and 300 K are shown in Fig. 2(a). Clear diamagnetic behavior is observed at both temperatures, which is an intrinsic property of silicon carbide. It should be noted that the deviation between the two curves is relatively small, which reveals that hardly any paramagnetic components are present in the pristine sample.

Figure 2(b) shows the M-H curves of CDC sample S3 measured at temperatures varying from 5 to 300 K. Clear diamagnetic components are also exhibited, which could originate from the SiC substrate and the CDC layers. Meanwhile, the resolvable overlaying hysteresis loop in the low magnetic field area (from about −4000 Oe to 4000 Oe) represents the existence of ferromagnetism. In contrast to the pristine sample, clear differences emerged between the the slopes of the M-H curves measured at different temperatures. Considering the rapid decline of paramagnetism with increasing temperature, the difference in curves acquired between 5 K and 300 K indicates the existence of paramagnetic components in the CDC sample. It should be noted that the intrinsic diamagnetic magnetization of graphitic materials is always temperature dependent [41], which can be used to explain the anomalous feature of the M-H curves between 100 K and 300 K and in turn to prove that the CDC layer is graphitized. Here, as an approximation, ignoring the small variation of diamagnetism between temperatures, the paramagnetic contribution in the high field area is achieved by subtracting the magnetization measured at 5 K from that of 300 K. The presence of paramagnetic centers in the CDC is also evidenced by ESR spectroscopy, which will be shown later. The paramagnetic contribution can be approximately expressed by using the Brillouin function:

$$M(x) = NJ\mu_B g_J \times \left[\frac{2J+1}{2J}\coth\left(\frac{2J+1}{2J}x\right) - \frac{1}{2J}\coth\left(\frac{1}{2J}x\right)\right], \quad (4)$$

where $M(x)$ represents the magnetization, μ_B is the Bohr magneton, J denotes the total angular momentum of the

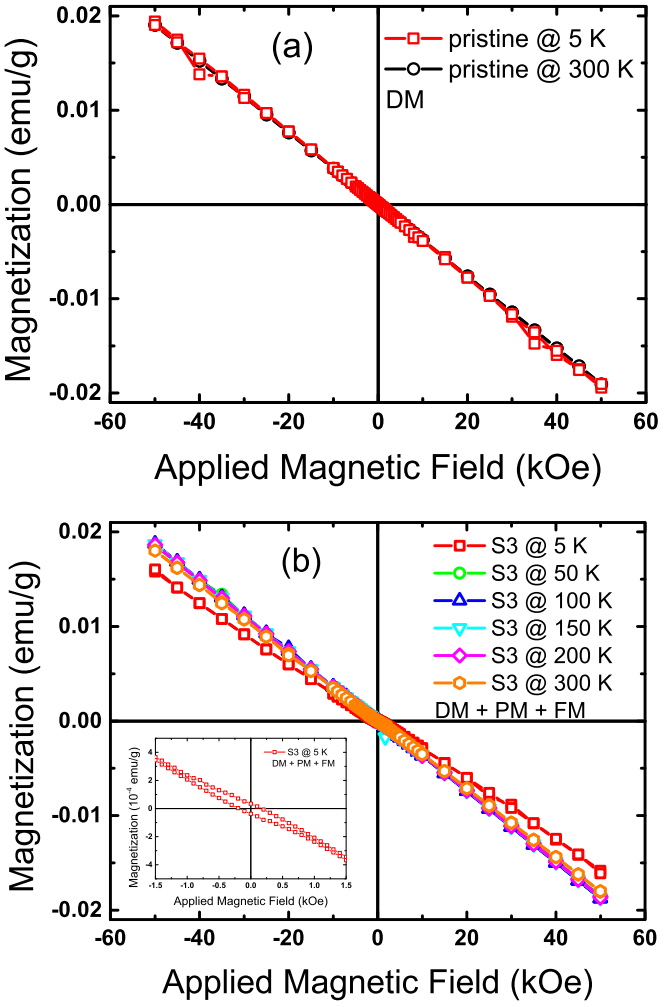

FIG. 2. (a) M-H curves of the pristine SiC sample measured at 5 K and 300 K; note that the deviation between two curves is relatively small. (b) M-H curves of CDC sample S3 measured at temperatures varying from 5 to 300 K. The resolvable overlaying hysteresis loop in the low magnetic field area (from approximately −4000 Oe to 4000 Oe and shown in the inset of the figure) represents the existence of ferromagnetism.

paramagnetic center, N is the density of local paramagnetic centers, H represents the magnetic field, T is the temperature, and g_J is the Landé factor, which is measured during the ESR experiment.

The paramagnetic component is fitted by the Brillouin function to calculate the values of J and N. The values and the standard error of N are calculated after specifying the value of J, and the best value of J is determined by choosing the minimum residual sum of squares between the fitting curves and experimental data. Here, the paramagnetic contribution is well fitted when J is equal to 1.3, with corresponding $N = 4.23 \times 10^{19} \pm 1.83 \times 10^{17}$ cm^{-3}. For other values of J, the fitted curves clearly deviate from the experimental results, as shown in Fig. 3(a).

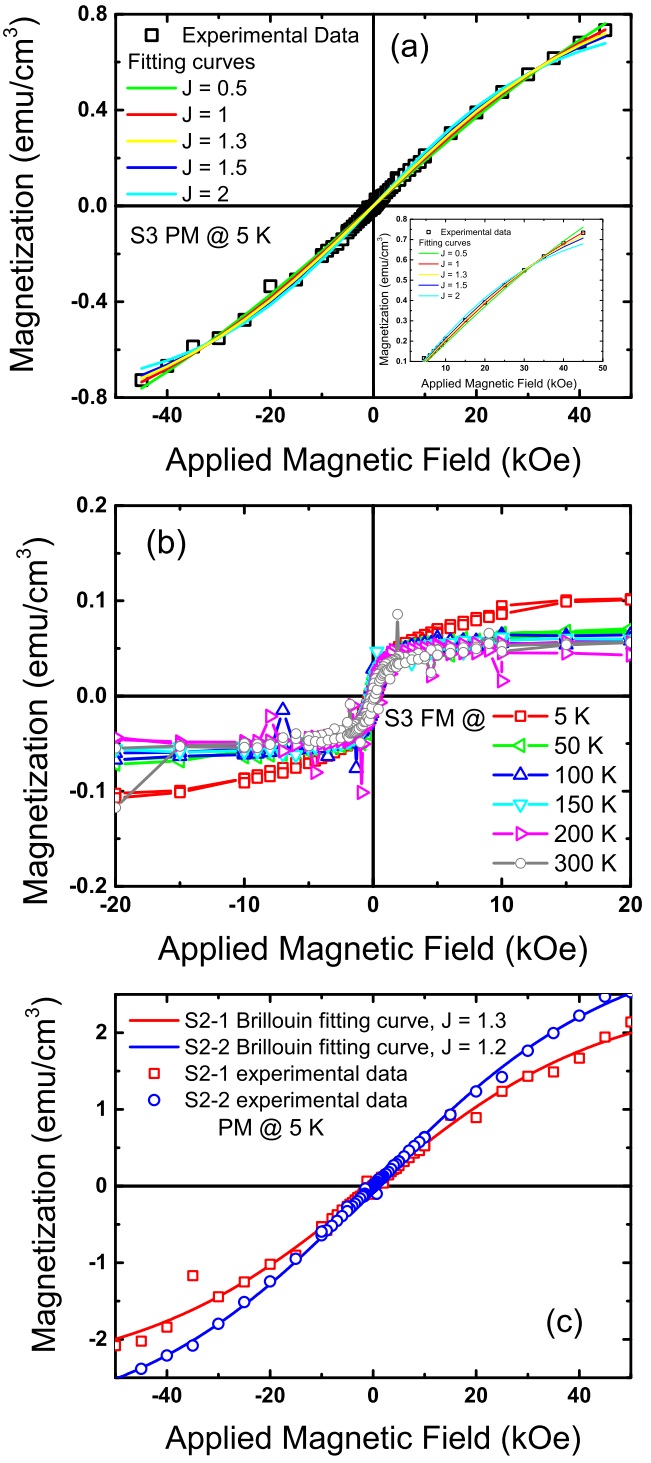

FIG. 3. (a) Brillouin fitting of the paramagnetic contribution of S3, which are achieved by subtracting the magnetization measured at 300 K from that at 5 K. The inset shows the zoomed-in region of the fitting curves at a high applied magnetic field (from 10 000 Oe to 50 000 Oe). (b) The ferromagnetic components of sample S3 at different measurement temperatures, which are achieved by subtracting the intrinsic diamagnetic components and the Brillouin paramagnetic components from the pristine measured M-H curves. (c) The paramagnetic contribution and the best Brillouin fitting curves with appropriate values of J for samples S2-1 and S2-2.

TABLE III. Brillouin fitting results for samples S2-1, S2-2, and S3. J represents the total angular momentum of the paramagnetic center, and N is the density of local paramagnetic centers.

Sample ID	J	N (cm^{-3})
S2-1	1.3	$1.13 \times 10^{20} \pm 8.10 \times 10^{17}$
S2-2	1.2	$1.57 \times 10^{20} \pm 4.45 \times 10^{17}$
S3	1.3	$4.23 \times 10^{19} \pm 1.83 \times 10^{17}$

The calculated value of J for CDC sample S3 indicates that the average total angular momentum of the CDC system and the real situation is a mixture of several kinds of paramagnetic centers with different values of total angular momentum due to the various types and concentrations of defects in CDC. We proposed a more detailed calculation on the defective sp^2 skeleton, which contains various defect types and concentrations, isolated spins, and a coupling energy difference between ferromagnetic and antiferromagnetic states, to reveal the relationship between the paramagnetic defects and ferromagnetic coupling in section E. Furthermore, the coexistence of paramagnetism and ferromagnetism was also reported in the context of defect-induced magnetism, such as that in SiC [42] and ZnO [43].

Figure 3(b) shows the M-H curves of sample S3 at different measurement temperatures with removal of the intrinsic diamagnetic components and the paramagnetic components. Because the magnetization measurements are based on the total volume of the samples, we assume that the ferromagnetic component originates from the CDC layer and the CDC-SiC interface and therefore that the average magnetization of the CDC layer can be estimated by normalizing the measured hysteresis loop with the volume of the CDC layer. Thus, the average saturation magnetization for the CDC layer is 0.75 emu/cm^3 at 5 K, and the coercive force is 350 Oe. Furthermore, as shown in Fig. 3(b), the average saturation magnetization decreases to 0.03 emu/cm^3 at room temperature, with a coercive force of 150 Oe. Figure 3(c) displays the paramagnetic contribution and the best Brillouin fitting curves with appropriate values of J for samples S2-1 and S2-2. There is a paramagnetic phase, but no ferromagnetism is observed. Moreover, our Brillouin fitting provides a result of $J = 1.3$, $N = 1.13 \times 10^{20} \pm 8.10 \times 10^{17}$ cm^{-3} for sample S2-1 and $J = 1.2$, $N = 1.57 \times 10^{20} \pm 4.45 \times 10^{17}$ cm^{-3} for Sample S2-2, as shown in Table III. For samples S2-1 and S2-2 prepared with a 120 min reaction time, if the linear reaction equation is used, the thickness of the CDC layer will be half of that of sample S3, and the number of local paramagnetic centers are 1.67 and 2.71 times larger, respectively, than that of S3. It should be noted that the density of paramagnetic centers obtained from the Brillouin fitting is on the same order as the concentration of defects estimated from the value of I_D/I_G in the Raman spectrum for sample S3. Additionally, the variation in paramagnetic centers between samples is consistent with the change in I_G. The difference in the density of local paramagnetic centers in the nonferromagnetic samples S2-1 and S2-2 and the ferromagnetic sample S3 demonstrates that the ferromagnetic phase probably appears upon total graphitization and with a smaller concentration of paramagnetic centers. Increasing the chlorination time will help reach this situation and induce the ferromagnetic component found in sample S3. Moreover, compared with the saturation magnetization measured in other graphite materials [23,44], the nanocrystalline graphite in the CDC layer of S3 will exhibit a more disordered state, which can explain the smaller magnetization value obtained in our sample. In addition, for sample S1 (for which the M-H curves are not shown), no ferromagnetic component is observed; instead, diamagnetism is observed due to the negative slope of the curve. An additional paramagnetic phase caused by the chlorination-induced defects can also be identified.

C. Electron spin resonance

ESR spectroscopy is performed to study the properties of the paramagnetic centers of the CDC sample. The ESR signals were calibrated using a standard Mn^{2+} marker sample. The ESR spectrum of the pristine 4H-SiC sample (which is not shown here) was measured at 120 K with the magnetic field perpendicular to the sample's surface, and the pristine sample did not present a clear signal in the ESR spectrum, which means that there is a tiny amount of paramagnetic centers in the sample, and showed the same features as previously reported in a high purity semi-insulating HPSI 4H-SiC sample [45].

Figure 4(a) shows the temperature evolution of the relative intensity of the ESR spectra for sample S3, measured with the magnetic field perpendicular to the sample surface. For all measured temperatures, broad and symmetric central lines of the derivative of the Lorentzian form lines are observed, and as an example, the spectrum measured at 80 K is shown in the inset of Fig. 4(a). The intensity of the EPR signal was the double integration of the pristine Lorentzian curve, and the EPR signals were normalized to the data measured at 300 K in order to compare the magnetic susceptibility. Because the paramagnetic signal of the original SiC wafer is weak, the signal measured here represents the magnetic response of the CDC layer after chlorination. For the chlorinated sample S3, the number of EPR centers measured by Bruker E500 with an internal spin number detector is $4.21(5) \times 10^{15}$. In order to have a better comparison with the Brillouin fitting results of the density of local paramagnetic centers listed in Table III, this value is also represented as the spin number per unit volume, which is $6.58(5) \times 10^{19}$ cm^{-3}. It revealed a nice correspondence between the ESR spin number and the Brillouin fitting result which is deduced from the SQUID measurement. The slight difference is due to the fitting process of achieving N. For instance, the small variation of diamagnetism between temperatures and the neglecting of the spin centers involved in ferromagnetism will cause N listed in Table III to be slightly smaller. This result proves that ESR detects all the spins in the chlorinated sample S3.

In addition, as shown in Fig. 4(a), the relative intensity is found to decrease with increasing temperature but shows a deviation from the utility of the Curie law, indicating that not only the paramagnetism was induced. It has been reported that the coupling of a large number of localized spin centers and a small number of conduction carriers gives a single Lorentzian-like ESR line in some carbon-based materials [46–49]. The observed G band in the Raman spectra demonstrates the existence of in-plane sp^2 carbon sites in our sample

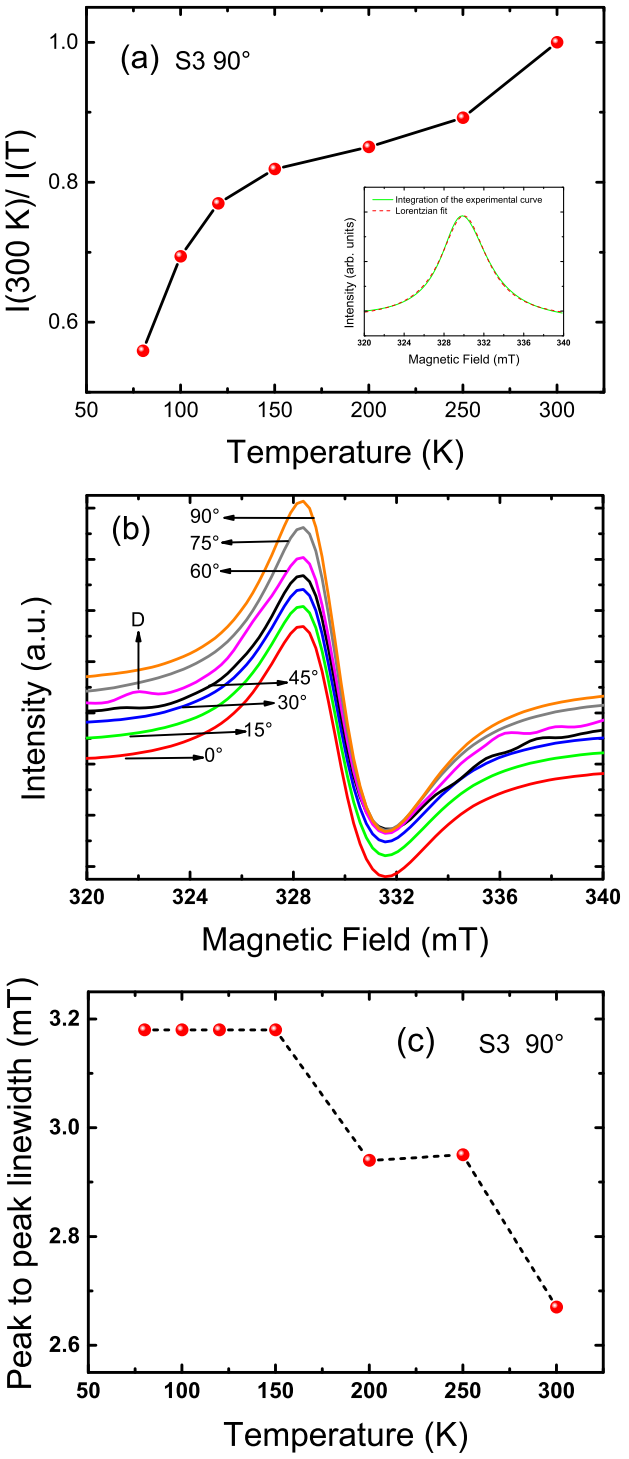

FIG. 4. (a) Temperature evolution of the relative intensity (normalized to the intensity measured at 300 K) of the ESR spectra for sample S3, measured with the magnetic field perpendicular to the sample surface. The integrated line of the intensity of the ESR spectrum of sample S3 fitted by a Lorentzian function (dashed line) taken at 80 K with the magnetic field perpendicular to the sample's surface is shown in the inset. (b) ESR spectra for chlorinated sample S3, measured at 80 K with the magnetic field rotated from perpendicular (90°) to parallel (0°) to the sample's surface. The arrow denotes the Dysonian form of the line shape at 60°. (c) The peak-to-peak linewidth as a function of temperature for sample S3, with the magnetic field perpendicular to the sample's surface.

as well as the conduction electrons. The observed values of g and ΔH_{pp} seem to be the sum of two parts based on the bottleneck approximation: $g = (g_1\chi_1 + g_2\chi_2)/(\chi_1 + \chi_2)$ and $\Delta H_{pp} = (\Delta H_{pp1}\chi_1 + \Delta H_{pp2}\chi_2)/(\chi_1 + \chi_2)$, where g_1 and χ_1 represent the contribution of Curie-type localized moments and g_2 and χ_2 represent the Pauli-type conduction electrons originating from the π electrons of the sp^2 hybrid carbon atoms. The Curie-type spin susceptibility is expressed as $\chi_1 = C/T$, where C is a constant, while the Pauli-type spin susceptibility (χ_2) is nearly temperature independent. However, due to the small number of conduction carriers, the effect of Pauli-type conduction electrons will be rather weak in our sample. For the anomalous temperature evolution tendency of the relative intensity, one possible origin is the magnetically correlated defects [4,50,51], which can be used to explain the appearance of the ferromagnetism in our CDC sample.

Figure 4(b) shows the ESR spectra for CDC sample S3 measured at 80 K with the magnetic field rotated from perpendicular to (90°) parallel to (0°) the sample's surface with a rotation step of 15°. For all measured angles, the Lorentzian form lines are preserved. The g value shows an isotropic property for all measured angles, which is approximately 1.994. The appearance of the isotropic g factor was also observed in doped or neutron-irradiated graphite, which would originate from the introduced defects [4,24].

The linewidth of the central Lorentzian peak (ΔH_{pp}) is approximately 3 mT at 80 K, which is larger than the measured values of amorphous carbon materials (0.25–1.5 mT) [12], carbon nanofoam (0.19–0.8 mT) [52], and polymerized C_{60} (<1 mT) [53–55]. However, the same magnitude was observed in multiwall carbon nanotubes (MWNT) [47–49], C_{60}^- [56] and some irradiated graphite samples (2.5–4 mT) [50].

The temperature evolution of the EPR linewidth shown in Fig. 4(c) can be interpreted as the slowing down of spin fluctuations due to developing spin correlations [57,58]. Thus, the two possible ESR broadening mechanisms, dipolar interaction and the exchange narrowing, should be considered. The enhanced dipolar interaction within dense paramagnetic centers needs the observation of a Gaussian ESR line shape [59], which is incompatible with the Lorentzian line shape observed in our experiment. It is noted that exchange narrowing averages the local fields from neighboring spins, which results in a narrowing of the linewidth and then partly exhibits the Lorentzian lineshape due to the finite lifetime [60]. It is therefore reasonable to deduce that the exchange narrowing explicating the main component of the ESR linewidth. The existence of exchange interaction provides positive evidence to the ferromagnetic component observed in the chlorinated sample [61].

In addition, for the detailed calculation, the contribution of the dipolar interaction between magnetic moments and the exchange narrowing to the ESR linewidth can be achieved from [59]: $\Delta B^d \approx \sqrt{\langle M_2 \rangle}/g\mu_B$ and $\Delta B^d \approx M_2/k_B J g\mu_B$. The second moment of the absorption line M_2 is given by: $M_2 = \frac{3}{4}\frac{\mu_0}{4\pi}^2 S(S+1)(g\mu_B)^4 \sum_k \frac{[3\cos^2\theta_{jk}-1]^2}{r_{jk}^6}$, where μ_0 is the vacuum permeability. The sum runs over all neighbors k of a given site j, connected by the vector r_{jk}. θ_{jk} is the angle between r_{jk} and the applied magnetic field [59]. However, due to the complex structure of the chlorinated layers and the distribution

of the defect, calculating the second moment of the absorption line (M_2) and the exchange narrowing to the ESR linewidth is beyond the scope of this study.

The ESR linewidth is also determined by subtle motional narrowing of the g-value distribution over the Fermi surface in graphite and decreases with the g-value anisotropy [62]. For our sample, the suppression of motional narrowing arose from the isotropic property of the g value can also lead to the increasing of linewidth with decreasing temperature and exhibits the Lorentzian lineshape. However, in this experiment, the EPR signal intensity shows the predominant contribution from the localized centers and the exchange narrowing accounts for the main component of the ESR linewidth.

Moreover, when the magnetic field is rotated to 60°, a Dysonian-like peak located at $\Delta H = 7.5$ mT from the central Lorentzian peak is also observed; however, the peak decreased at an angle of 45° and disappeared at other angles, which is different from the phenomenon observed in graphite materials, in which the intensity of the Dysonian-like peak is comparable with the Lorentzian peak and changes continuously with the angle [24]. The anisotropy of the Dysonian-like peak is possibly due to the rather different structures of the amorphous CDC and the crystalline graphite.

D. Ferromagnetic resonance

Here, we comment on the ferromagnetic resonance experiment which was performed at several frequencies over the range of 3–17 GHz at room temperature for sample S3. During the measurement, the magnetic field was applied in the film plane. For the low frequency microwaves (3–10 GHz), a small resonance field is expected. In this case, the difference between the Zeeman splitting of the energy levels (also the equilibrium population difference between the energy levels) for an electron will be rather small, especially at the temperature which is not low enough. Therefore, the power absorption is so weak that beyond the detection limit of the FMR instrument and the results are not shown here. However, the absorption can be observed at high frequency (11–17 GHz) region at room temperature, as shown in Fig. 5(a). A linear relationship between the resonance field (H_{res}) and the frequency of the microwave (f) is extracted, as depicted in Fig. 5(b). The magnetization dynamics in FMR is described by the Landau-Lifshitz equation if the Gilbert damping is neglected [63]:

$$\frac{d\boldsymbol{M}}{dt} = \gamma(\boldsymbol{M} \times \boldsymbol{B}_0^{'}), \tag{5}$$

where $\boldsymbol{M}$ is the magnetization vector, and γ is the gyromagnetic ratio. Furthermore, the resonance frequency and the resonance field can be linked through the Kittle equation. If the demagnetizing tensor and the magnetocrystalline anisotropy are considered, the resonance frequency is given by [63,64]:

$$f_{\text{res}} = \left(\frac{\gamma}{2\pi}\right)\{[H_{\text{res}} + (N_x - N_z)4\pi M_{\text{eff}}] \times [H_{\text{res}} + (N_y - N_z)4\pi M_{\text{eff}}]\}^{\frac{1}{2}} \tag{6}$$

in which M_{eff} is the effective magnetization which contains the saturation magnetization and the anisotropy contributions

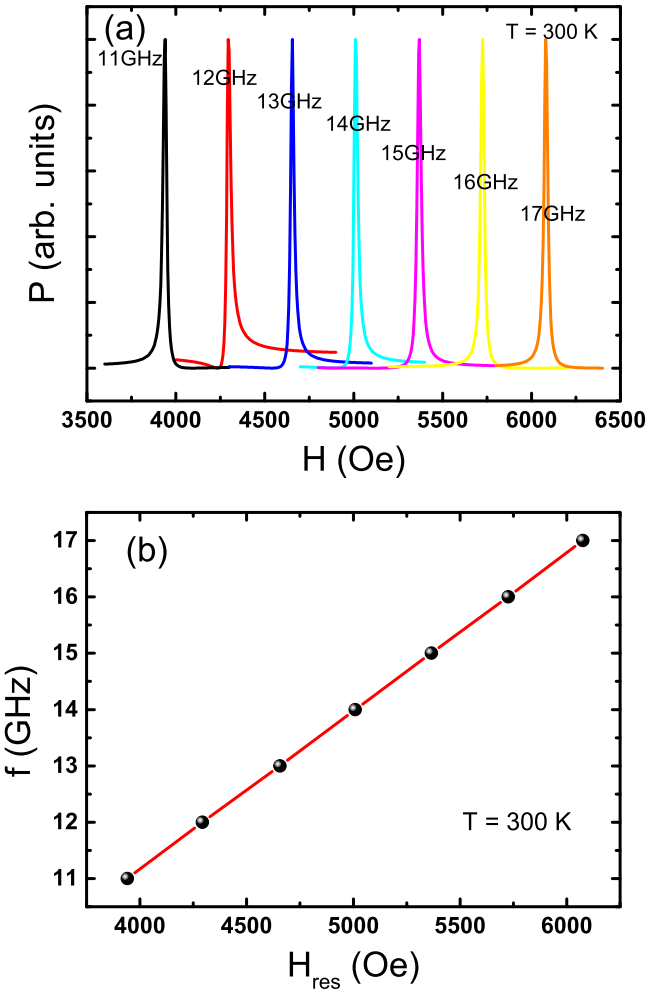

FIG. 5. (a) Ferromagnetic resonance spectra of the absorption for the CDC film S3 at gigahertz frequencies of 11, 12, 13, 14, 15, 16, and 17 GHz at room temperature. (b) The frequencies versus the resonance magnetic field curve at 300 K. The f_{res}-H_{res} curve is linear at the high frequency (11–17 GHz) region.

in Gauss system of units. For a thin film with applied field in plane,

$$f_{\text{res}} = \left(\frac{\gamma}{2\pi}\right)[(H_{\text{res}} + 4\pi M_{\text{eff}})H_{\text{res}}]^{\frac{1}{2}}, \tag{7}$$

the nonlinear relationship between f_{res} and H_{res} was used to provide convincing evidence on the ferromagnetism in the measured sample [65]. However, when H_{res} is much larger than the value of $4\pi M_{eff}$, the relationship between f_{res} and H_{res} degenerate into linear. For our experiment, compared with the H_{res}, the value of $4\pi M_{eff}$ (contain the saturation magnetization and the anisotropy contributions) is too small to make the f_{res}-H_{res} curve a deviation from the linear relationship at high frequency region. For example, ignoring the small anisotropy contributions, the value of $4\pi M_{sat}$ is about 0.01% of f_{res} at 11 GHz. Moreover, according to the slope of the f_{res}-H_{res} curve, the gyromagnetic ratio and the g value can be calculated; the result shows no difference from that which we obtained from the ESR measurement. For the chlorinated sample in our experiment, it is hard to distinguish the FM coupling from

the FMR experiment when the power absorption at the low frequency region (3–10 GHz) is rather weak.

E. Discussion

According to our previous magnetic measurement and ESR results, paramagnetism and ferromagnetism are observed simultaneously in CDC layers. This phenomenon was also found in other TM-free materials that exhibit defect-induced ferromagnetism, and thus, interaction between paramagnetic centers may play a vital role in the ferromagnetic properties of the CDC sample. To better understand this issue, we discuss the relationship between paramagnetic centers and ferromagnetic coupling in CDC layers through some first-principles calculations in this section. To match the experimental procedure and simplify the model, this section is divided into two parts. First, a CDC-4H-SiC surface model was developed to explain the formation of the graphitic layers and the transformation from sp^3 bonds to the planar sp^2 configuration when the Si atoms are removed from the 4H-SiC crystals, as revealed by the Raman spectra. Then, the magnetic properties, for example, the moment, the spin-polarization energy, and the energy difference between the ferromagnetic and antiferromagnetic states of the defective graphitic layers with several different configurations, were calculated to explain the magnetism in the SiC-CDC layers.

The calculations were performed using the Cambridge Serial Total Energy Package (CASTEP). Spin-polarized electronic structure calculations were carried out by using the Perdew-Burke-Ernzerhof (PBE) functional [66] for the exchange-correlation potential under the generalized gradient approximation (GGA). The ultrasoft pseudopotential was used for the interactions between electrons and ions. The cutoff energy for the plane-wave basis set was set to 400 eV, and appropriate Monkhorst-Pack k-point meshes were used for integrations of the reduced Brillouin zone. The lattice constants and internal coordinates were relaxed with the Broyden-Fletcher-Goldfarb-Shanno (BFGS) optimization method. The change of energy, maximum tolerance of the force, maximum stress, and maximum displacement were set to 2×10^{-5} eV/atom, 0.05 eV/Å, 0.1 Gpa, and 2×10^{-3} Å, respectively.

1. Structural transformation

A 2×2 surface supercell with four double layers and a 12 Å vacuum was built, and a gradient SiC-CDC interface structure model was achieved by removing two Si atoms from the outermost atomic layer and one Si atom from the atomic sublayer of a 4H-SiC crystal. The primitive cell of 4H-SiC has lattice constants $a = b = 3.078$ Å and $c = 10.046$ Å with a space group $P63mc$. We calculated the formation energy of the system when it is spin polarized, which therefore provides the local moment. After geometrical optimization, we found that the carbon atoms tend to form a planar structure in the outermost layer and the sublayer, which indicates the conversion of the tetrahedral sp^3 bonds into planar sp^2 bonds. The schematic diagrams for the surface structure model before and after optimization are shown in Fig. 6. A net magnetic moment of 0.83 μ_B indicates that the transformation is available when

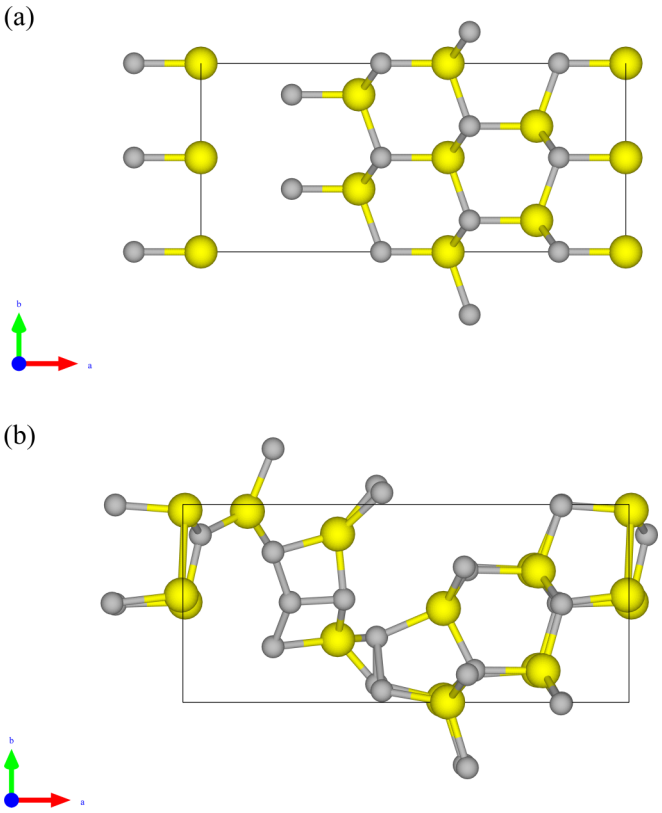

FIG. 6. A 2×2 surface supercell model with four double layers and a 12 Å vacuum (a) before and (b) after geometrical optimization. After geometrical optimization, the carbon atoms tend to form a planar structure in the outermost layer and the sublayer.

the system is spin polarized. The same phenomenon was also observed in a 3C-SiC/CDC interface [67].

2. Magnetic property

Because of the graphitic property of the CDC layers revealed by the Raman spectra, the abnormal diamagnetism, the structural transformation proved by previous calculations and the defective graphite can be used as a simplified model to illustrate the ferromagnetism in CDC layers. By building the model of defects that occupy different numbers of carbon atoms and choosing the distance between them, we can find the appropriate type and density of defects in the sp^2 skeleton to induce paramagnetism and ferromagnetism. The primitive cell of graphite used in our calculations features lattice constants $a = b = 2.46$ Å and $c = 6.70$ Å. As shown in Fig. 7, 12 different types of vacancies in the graphite layers were built and investigated in this study. The term Vn is used to label the number of the lost carbon atoms in the planar ring structure. For V1, V5, and V6, there is only one configuration, while for V2, V3, and V4, there are three structures for each kind. The energy difference between the spin-unpolarized and spin-polarized states (ΔE_{sp}) of each configuration is first calculated to investigate the observed paramagnetism. The spin-polarization energies as a function of the distance between defects (d_v) are shown in Table II and Fig. 8(a).

The distance is calculated from the volume of the corresponding supercell, and it also represents the concentration of

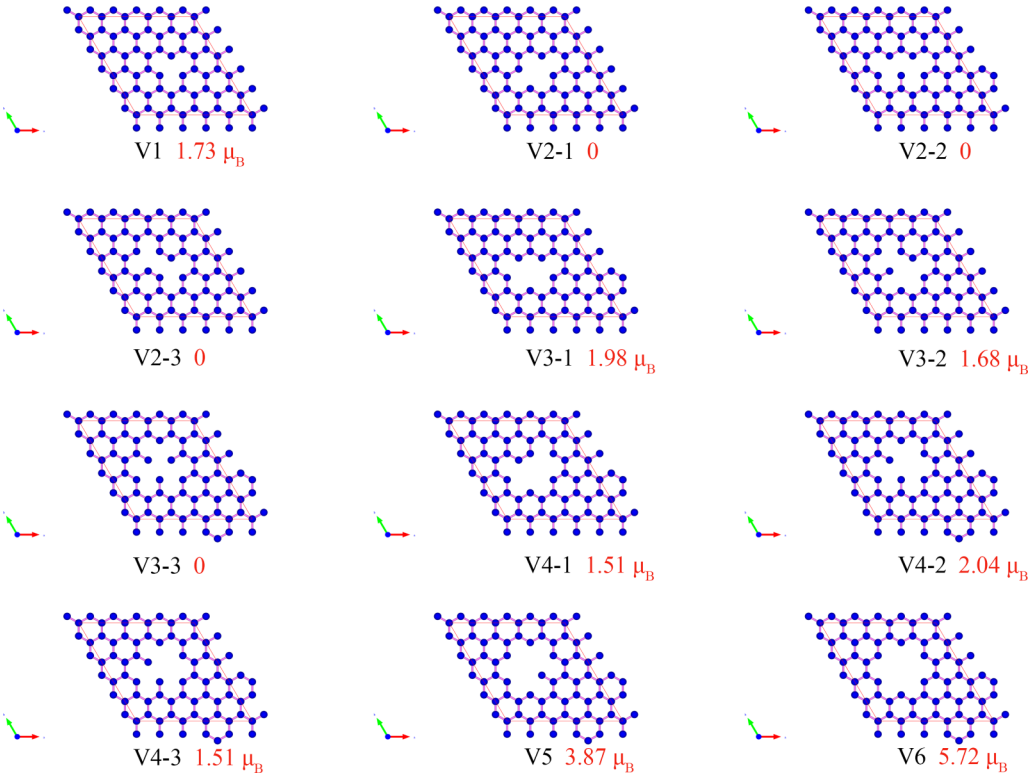

FIG. 7. Twelve different configurations of vacancies in graphite layers, labeled with V1, V2, V3, V4, V5, and V6 according to the number of the lost carbon atoms in the planar ring structure. For V1, V5, and V6, there is only one configuration, while for V2, V3, and V4, there are three configurations for each type. The calculated moment of each configuration is also shown in the figure.

defects. The calculated spin-polarization energies are summarized in Table IV. The moments for V1, V3-1, V3-2, V4-1, V4-3, V5, and V6 are found to be nonzero. However, the ΔE_{sp} for V5 changes drastically with distance, which means that this configuration is not stable. Meanwhile, the variation tendency is different for each configuration. As shown in Fig. 8(a), for V1, V4-1, V4-3, and V6, ΔE_{sp} decreases when d_v increases, demonstrating that the spin polarization is stable at high concentrations. However, for V3-1 and V3-2, ΔE_{sp} increases with vacancy separation, indicating that the spin polarization is stable at low concentrations. In addition, compared with the other configurations, the ΔE_{sp} of V4-2 and V6 are lower at long distances, while the ΔE_{sp} of V4-2 and V3-2 are lower at short distances. The values of concentration corresponding to the $5 \times 5 \times 1$ and $6 \times 6 \times 1$ supercells are 9.86×10^{20} cm^{-3} and 6.85×10^{20} cm^{-3}, respectively, which are near the density of paramagnetic centers (N) obtained from the Brillouin fitting in our chlorinated samples if we consider the effects of the surface and interface region in the real experiments. This result indicates that the low concentration state is suitable and that the V4-2 and V6 defects would be the dominant defects in the graphitic CDC films. Furthermore, because the value of J does not change between samples, the dominant configuration of defects is constant, and the decrease in N is attributable to the reduction in the number of defects. Additionally, the existence of a large number of V4-2 and a small number of V6 in CDC can lead to an average moment of approximately 2.5 μ_B, as evidenced by the Brillouin fitting. Previous investigations [68,69] using the plane wave basis Vienna *ab initio* simulation package (VASP) and the GGA and projected augmented wave potentials reveals the magnetic states of V1, V4, and V6 are all in the ground state. The V1 defect occupies a magnetic moment of 1.04 μ_B, whereas each V6 with a planar ring structure induces a ~5.54 μ_B local magnetic moment, and each V4 defect induces a ~1.97 μ_B local magnetic moment. These results are close to the values from our calculations.

In addition, the energy difference between the antiferromagnetic and ferromagnetic phases of the stable defects with nonzero local moments (V1, V3-1, V3-2, V4-2, and V6) are calculated to investigate the magnetic coupling. We put two supercells side by side along the xy plane with each of the supercells containing one defect. The interaction between defects along the z plane is not discussed in this subsection due to the rather weak coupling between them. The ΔE_{FA} values of these defects are listed in Table IV, and the energy difference as a function of the distance between defects is depicted in Fig. 8(b). The ΔE_{FA} is strongly dependent on the configuration of defects. For example, the V4-2 defect favors a ferromagnetic coupling ($\Delta E_{FA} = -285.42$ meV) when the d_V values are 12.30 Å and 14.76 Å, whereas the rest of the ΔE_{FA} for other distances is near zero and positive. The V6 defects antiferromagnetically couples with each other at all distances and occupies a maximal ΔE_{FA} of 806.64 meV when d_V is 9.84 Å. In the mean field approximation, the Curie temperature of the system is calculated as $2k_BT_C = 3J(d_V)$. By using a nearest-neighbor Heisenberg model, the value of $J(d_V)$ can be calculated as $J(d_V) = -\Delta E_{FA}/4S^2$ in our supercell.

TABLE IV. Calculating the results of spin-polarization energy and the energy difference between the ferromagnetic and antiferromagnetic phases ($\Delta E_{FA} = E_{\text{ferromagnetism}} - E_{\text{antiferromagnetism}}$) of different configurations. The value of d_v represents the distance between defects. For the calculation of ΔE_{FA}, two supercells are side by side along the xy plane, and each of the supercells contains one defect.

Configuration	d_V (Å)	ΔE_{sp} (meV)	ΔE_{FA} (meV)
V1	4.92	−169.00	−167.43
	7.38	−164.70	−63.74
	9.84	−440.78	−22.09
	12.30	−277.65	−58.69
	14.76	−490.96	−4.06
V2-1	4.92	−0.13	
	7.38	−3.12	
	9.84	4.42	
	12.30	−46.82	
	14.76	20.22	
V2-2	4.92	−31.63	
	7.38	38	
	9.84	−15.79	
	12.30	−103.34	
	14.76	−123.05	
V2-3	4.92	6.9	
	7.38	59	
	9.84	−3.32	
	12.30	−95	
	14.76	−199.48	
V3-1	7.38	−504.29	−33.07
	9.84	−580.27	−580.27
	12.30	−674.56	−674.56
	14.76	−390.73	−390.73
V3-2	7.38	−552.39	−552.39
	9.84	−564.86	−564.86
	12.30	−455.32	−455.32
	14.76	−291.95	−291.95
V3-3	7.38	−184.56	
	9.84	−671.84	
	12.30	3971.2	
	14.76	7566.6	
V4-1	7.38	187.52	
	9.84	−302.80	
	12.30	−328.85	
	14.76	−349.7	
V4-2	7.38	−1229.45	0.64
	9.84	−830.90	346.08
	12.30	−1503.97	−285.42
	14.76	−834.97	−2.94
V4-3	7.38	20.91	
	9.84	−57.56	
	12.30	−146.1	
	14.76	−354.25	
V5	7.38	594.62	
	9.84	−447.60	
	12.30	−355.5	
	14.76	799.29	
V6	7.38	1485.74	25.32
	9.84	−503.15	806.64
	12.30	−1434.52	510.14
	14.76	−1262.71	531.47

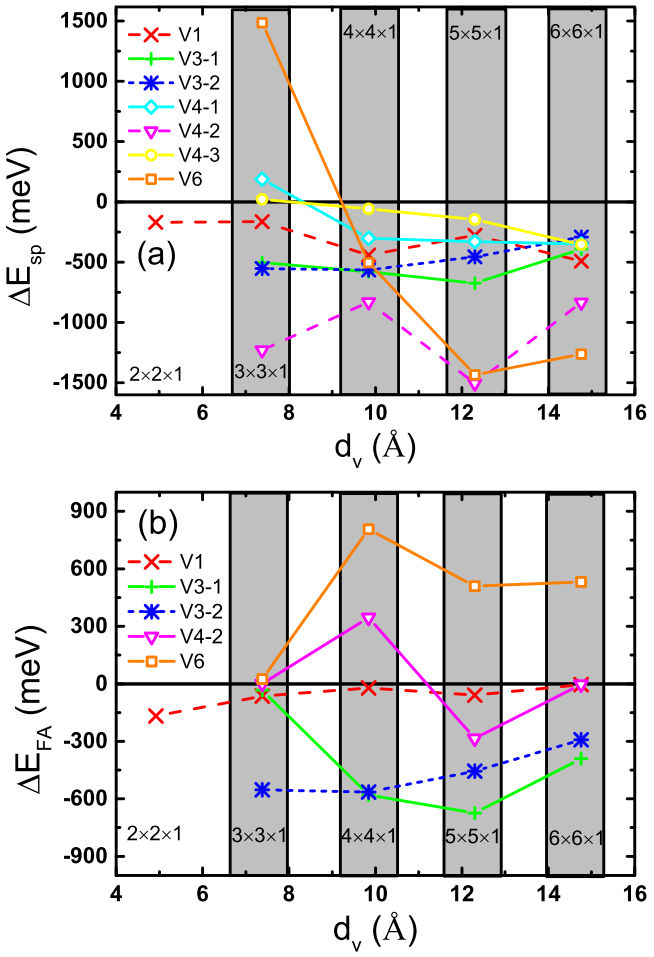

FIG. 8. (a) The spin-polarization energy as a function of the distance between defects (d_v) and (b) the energy difference between the antiferromagnetic and ferromagnetic phases as a function of distance. The corresponding supercells are also shown in the figure.

As a result, the calculated values of $J(d_V)$ and T_C for the V4-2 configuration are 17.84 meV and 310.5 K, respectively, which indicate a room temperature ferromagnetic order. The value of ΔE_{FA} is observed to be sensitive to the concentration of defects, and when d_V is less than 12.30 Å, the energy difference between the antiferromagnetic and ferromagnetic phases increases rapidly as d_V decreases. By contrast, for a larger d_V, the growth rate for as d_V increases is almost half of the previous one. As revealed by the Raman spectra and the Brillouin fitting, the densities of the defects and the paramagnetic centers are decreased with increasing chlorination time, and the 4 h chlorination time induces the formation of a proper concentration of paramagnetic defects. This subtle difference in defect concentration can help us understand the appearance of ferromagnetic coupling in S3 and the absence of ferromagnetism in S2-1 and S2-2. Furthermore, the ferromagnetic signal is also observed in the sample that has the same chlorination time but a slightly different temperature (1000 °C) in our experiments. The above facts also link the reaction time with the ferromagnetic order and the concentration of defects. The defect concentration dependence of the energy

difference between the antiferromagnetic and ferromagnetic phases is also observed in SiC, graphene and graphite ribbons, for example, the ΔE_{FA} of $V_{Si}V_C$ divacancy with different charge states [42].

IV. CONCLUSION

In conclusion, TM-free silicon CDC has been prepared, and its structural and magnetic properties have been measured and analyzed. Raman spectroscopic analysis reveals graphitic CDC films generated with etching times of 120 min and 240 min in a chlorine-containing environment. The paramagnetic and ferromagnetic components are separated from the measured magnetization-magnetic field curves of the samples. With the use of a Brillouin fitting, paramagnetic centers carrying a local magnetic moment of $\sim$1.3 μ_B are observed in these samples. A resolvable hysteresis loop in the low magnetic field area (from approximately $-$4000 Oe to 4000 Oe) with a saturation magnetization of 0.1 emu/cm^3 at 5 K and a coercive force of $\sim$300 Oe is observed in one of the chlorinated samples. The saturation magnetization decreases to 0.06 emu/cm^3 at room temperature, with a coercive force of 150 Oe. The temperature dependence of the relative intensity and the peak-to-peak linewidth of the Lorentzian-like ESR line observed by electron spin spectroscopy reveal the existence of an exchange interaction between the localized paramagnetic centers. We comment on the ferromagnetic resonance experiment which was performed at several frequencies over the range of 3–17 GHz at room temperature for sample S3. First-principles calculations indicate a conversion of tetrahedral sp^3 bonds into planar sp^2 bonds and reveal the dominant configuration of defects in the graphitic CDC films. Additionally, by calculating the energy difference between the antiferromagnetic and ferromagnetic phases, we deduce that the ferromagnetic coupling depends on the concentration of defects. This work will help us understand the appearance and the absence of ferromagnetism in these CDC samples.

ACKNOWLEDGMENTS

The work is financially supported by the National Natural Science Foundation of China (Grants No. 51472196, and No. 61604118) and the National Key Research and Development Program of China (Grant No. 2016YFB0400500). The author thanks the Beijing Shuruikechuang Technology Co., Ltd., and B.X. Shu for their assistance. B.P. also gratefully acknowledges discussions with Dr. K. Wang, Prof. Y.M. Zhang, and Prof. G.D. Lu for their selfless help.

[1] P. Esquinazi, D. Spemann, R. Höhne, A. Setzer, K.-H. Han, and T. Butz, Phys. Rev. Lett. **91**, 227201 (2003).
[2] H. Pardo, R. Faccio, F. Araújo-Moreira, O. De Lima, and A. Mombrú, Carbon **44**, 565 (2006).
[3] J. Cervenka, M. Katsnelson, and C. Flipse, Nat. Phys. **5**, 840 (2009).
[4] Z. He, X. Yang, H. Xia, X. Zhou, M. Zhao, Y. Song, and T. Wang, Carbon **49**, 1931 (2011).
[5] C. Rao, H. R. Matte, K. Subrahmanyam, and U. Maitra, Chem. Sci. **3**, 45 (2012).
[6] G. Ning, C. Xu, L. Hao, O. Kazakova, Z. Fan, H. Wang, K. Wang, J. Gao, W. Qian, and F. Wei, Carbon **51**, 390 (2013).
[7] T. L. Makarova, K.-H. Han, P. Esquinazi, R. Da Silva, Y. Kopelevich, I. Zakharova, and B. Sundqvist, Carbon **41**, 1575 (2003).
[8] A. N. Andriotis, M. Menon, R. M. Sheetz, and L. Chernozatonskii, Phys. Rev. Lett. **90**, 026801 (2003).
[9] S. Mathew, B. Satpati, B. Joseph, B. N. Dev, R. Nirmala, S. K. Malik, and R. Kesavamoorthy, Phys. Rev. B **75**, 075426 (2007).
[10] K. W. Lee, H. Kweon, and C. E. Lee, Adv. Mater. **25**, 5663 (2013).
[11] K. Tanaka, M. Kobashi, H. Sanekata, A. Takata, T. Yamabe, S. Mizogami, K. Kawabata, and J. Yamauchi, J. Appl. Phys. **71**, 836 (1992).
[12] K. Murata and H. Ushijima, J. Appl. Phys. **79**, 978 (1996).
[13] Y. Kopelevich, R. R. da Silva, J. H. S. Torres, A. Penicaud, and T. Kyotani, Phys. Rev. B **68**, 092408 (2003).
[14] R. Höhne, K.-H. Han, P. Esquinazi, A. Setzer, H. Semmelhack, D. Spemann, and T. Butz, J. Magn. Magn. Mater. **272–276**, E839 (2004).
[15] A. V. Rode, E. G. Gamaly, A. G. Christy, J. G. F. Gerald, S. T. Hyde, R. G. Elliman, B. Luther-Davies, A. I. Veinger, J. Androulakis, and J. Giapintzakis, Phys. Rev. B **70**, 054407 (2004).
[16] N. Parkansky, B. Alterkop, R. Boxman, G. Leitus, O. Berkh, Z. Barkay, Y. Rosenberg, and N. Eliaz, Carbon **46**, 215 (2008).
[17] N. Souza, S. Sergeenkov, C. Speglich, V. Rivera, C. Cardoso, H. Pardo, A. Mombru, A. Rodrigues, O. De Lima, and F. Araujo-Moreira, Appl. Phys. Lett. **95**, 233120 (2009).
[18] I. Felner and E. Prilutskiy, J. Supercond. Nov. Magn. **25**, 2547 (2012).
[19] J. Černák, G. Helgesen, A. T. Skjeltorp, J. Kováč, J. Voltr, and E. Čižmár, Phys. Rev. B **87**, 014434 (2013).
[20] O. V. Yazyev and L. Helm, Phys. Rev. B **75**, 125408 (2007).
[21] P. O. Lehtinen, A. S. Foster, Y. Ma, A. V. Krasheninnikov, and R. M. Nieminen, Phys. Rev. Lett. **93**, 187202 (2004).
[22] Y. Zhang, S. Talapatra, S. Kar, R. Vajtai, S. K. Nayak, and P. M. Ajayan, Phys. Rev. Lett. **99**, 107201 (2007).
[23] H. Ohldag, P. Esquinazi, E. Arenholz, D. Spemann, M. Rothermel, A. Setzer, and T. Butz, New J. Phys. **12**, 123012 (2010).
[24] K. W. Lee and C. E. Lee, Phys. Rev. Lett. **97**, 137206 (2006).
[25] J. Barzola-Quiquia, P. Esquinazi, M. Rothermel, D. Spemann, T. Butz, and N. García, Phys. Rev. B **76**, 161403 (2007).
[26] P. Esquinazi, W. Hergert, D. Spemann, A. Setzer, and A. Ernst, IEEE T. Magn. **49**, 4668 (2013).
[27] R. Nair, M. Sepioni, I.-L. Tsai, O. Lehtinen, J. Keinonen, A. Krasheninnikov, T. Thomson, A. Geim, and I. Grigorieva, Nat. Phys. **8**, 199 (2012).
[28] Y. Korenblit, M. Rose, E. Kockrick, L. Borchardt, A. Kvit, S. Kaskel, and G. Yushin, Acs Nano **4**, 1337 (2010).
[29] D. A. Ersoy, M. J. McNallan, and Y. Gogotsi, Mater. Res. Innovations **5**, 55 (2001).
[30] S. Urbonaite, L. Hälldahl, and G. Svensson, Carbon **46**, 1942 (2008).

[31] A. C. Ferrari and J. Robertson, Phys. Rev. B **61**, 14095 (2000).
[32] Z. Cambaz, G. Yushin, Y. Gogotsi, K. Vyshnyakova, and L. Pereselentseva, J. Am. Ceram. Soc. **89**, 509 (2006).
[33] B. Song, X. Chen, J. Han, G. Wang, H. Bao, L. Duan, K. Zhu, H. Li, Z. Zhang, W. Wang *et al.*, J. Magn. Magn. Mater. **323**, 2876 (2011).
[34] J. C. Burton, L. Sun, F. H. Long, Z. C. Feng, and I. T. Ferguson, Phys. Rev. B **59**, 7282 (1999).
[35] D. Roy, M. Chhowalla, H. Wang, N. Sano, I. Alexandrou, T. Clyne, and G. Amaratunga, Chem. Phys. Lett. **373**, 52 (2003).
[36] M. Pimenta, G. Dresselhaus, M. S. Dresselhaus, L. Cancado, A. Jorio, and R. Saito, Phys. Chem. Chem. Phys. **9**, 1276 (2007).
[37] F. Tuinstra and J. L. Koenig, J. Chem. Phys. **53**, 1126 (1970).
[38] Y. Wang, P. Pochet, C. A. Jenkins, E. Arenholz, G. Bukalis, S. Gemming, M. Helm, and S. Zhou, Phys. Rev. B **90**, 214435 (2014).
[39] B. S. Elman, M. Shayegan, M. S. Dresselhaus, H. Mazurek, and G. Dresselhaus, Phys. Rev. B **25**, 4142 (1982).
[40] Z. He, H. Xia, X. Zhou, X. Yang, Y. Song, and T. Wang, J. Phys. D: Appl. Phys. **44**, 085001 (2011).
[41] Z. Li, L. Chen, S. Meng, L. Guo, J. Huang, Y. Liu, W. Wang, and X. Chen, Phys. Rev. B **91**, 094429 (2015).
[42] Y. Wang, Y. Liu, E. Wendler, R. Hübner, W. Anwand, G. Wang, X. Chen, W. Tong, Z. Yang, F. Munnik, G. Bukalis, X. Chen, S. Gemming, M. Helm, and S. Zhou, Phys. Rev. B **92**, 174409 (2015).
[43] J. B. Yi, C. C. Lim, G. Z. Xing, H. M. Fan, L. H. Van, S. L. Huang, K. S. Yang, X. L. Huang, X. B. Qin, B. Y. Wang, T. Wu, L. Wang, H. T. Zhang, X. Y. Gao, T. Liu, A. T. S. Wee, Y. P. Feng, and J. Ding, Phys. Rev. Lett. **104**, 137201 (2010).
[44] J. C. C. Freitas, W. L. Scopel, W. S. Paz, L. V. Bernardes, F. E. Cunha-Filho, C. Speglich, F. M. Araújo-Moreira, D. Pelc, T. Cvitanić, and M. Požek, Sci. Rep. **5**, 14761 (2015).
[45] R.-W. Zhou, X.-C. Liu, H.-J. Wang, W.-B. Chen, F. Li, S.-Y. Zhuo, and E.-W. Shi, AIP Adv. **5**, 047146 (2015).
[46] S. Mrozowski, Carbon **6**, 841 (1968).
[47] F. Beuneu, C. L'Huillier, J.-P. Salvetat, J.-M. Bonard, and L. Forró, Phys. Rev. B **59**, 5945 (1999).
[48] V. Likodimos, S. Glenis, N. Guskos, and C. L. Lin, Phys. Rev. B **68**, 045417 (2003).
[49] J. P. Salvetat, T. Fehér, C. L'Huillier, F. Beuneu, and L. Forró, Phys. Rev. B **72**, 075440 (2005).
[50] K. W. Lee, H. Kweon, J. Kweon, and C. E. Lee, J. Appl. Phys. **107**, 044302 (2010).
[51] X. He and J. Tan, Physica E **93**, 6 (2017).
[52] D. Arčon, Z. Jagličič, A. Zorko, A. V. Rode, A. G. Christy, N. R. Madsen, E. G. Gamaly, and B. Luther-Davies, Phys. Rev. B **74**, 014438 (2006).
[53] O. Chauvet, G. Oszlànyi, L. Forro, P. W. Stephens, M. Tegze, G. Faigel, and A. Jànossy, Phys. Rev. Lett. **72**, 2721 (1994).
[54] C. Knapp, K.-P. Dinse, B. Pietzak, M. Waiblinger, and A. Weidinger, Chem. Phys. Lett. **272**, 433 (1997).
[55] J. Stankowski, L. Piekara-Sady, W. Kempiński, O. Huminiecki, and P. B. Sczaniecki, Fullerene Sci. Technol. **5**, 1203 (1997).
[56] P. Allemand, G. Srdanov, A. Koch, K. Khemani, F. Wudl, Y. Rubin, F. Diederich, M. Alvarez, S. Anz, and R. Whetten, J. Am. Chem. Soc. **113**, 2780 (1991).
[57] A. Zorko, M. Pregelj, H. Luetkens, A.-K. Axelsson, and M. Valant, Phys. Rev. B **89**, 094418 (2014).
[58] S. Zimmermann, F. Steckel, C. Hess, H. W. Ji, Y. S. Hor, R. J. Cava, B. Büchner, and V. Kataev, Phys. Rev. B **94**, 125205 (2016).
[59] D. Gatteschi and A. Bencini, *Electron Paramagnetic Resonance of Exchange Coupled Systems* (Springer, Berlin, 1990).
[60] S. Just, S. Zimmermann, V. Kataev, B. Büchner, M. Pratzer, and M. Morgenstern, Phys. Rev. B **90**, 125449 (2014).
[61] A. Zorko, M. Pregelj, M. Gomilšek, Z. Jagličić, D. Pajić, M. Telling, I. Arčon, I. Mikulska, and M. Valant, Sci. Rep. **5**, 7703 (2015).
[62] S. Mrozowski, Carbon **3**, 305 (1965).
[63] J. M. Coey, *Magnetism and Magnetic Materials* (Cambridge University Press, Cambridge, 2010).
[64] Y. Zhao, Q. Song, S.-H. Yang, T. Su, W. Yuan, S. S. Parkin, J. Shi, and W. Han, Sci. Rep. **6**, 22890 (2016).
[65] Y. Liu, Y. Yuan, F. Liu, R. Böttger, W. Anwand, Y. Wang, A. Semisalova, A. N. Ponomaryov, X. Lu, E. Arenholz *et al.*, Phys. Rev. B **95**, 195309 (2017).
[66] J. P. Perdew, K. Burke, and M. Ernzerhof, Phys. Rev. Lett. **77**, 3865 (1996).
[67] H. Jin, R. Zhang, and Q. Liu, Mater. Lett. **64**, 1019 (2010).
[68] Y. Ma, P. Lehtinen, A. S. Foster, and R. M. Nieminen, New J. Phys. **6**, 68 (2004).
[69] X. Yang, H. Xia, X. Qin, W. Li, Y. Dai, X. Liu, M. Zhao, Y. Xia, S. Yan, and B. Wang, Carbon **47**, 1399 (2009).